

Electrochemically induced metal- vs. ligand-based redox changes in mackinawite: identification of a Fe^{3+} - and polysulfide-containing intermediate†

Sebastian A. Sanden,^{id}*^{a,b} Robert K. Szilagy,^{id}*^c Yamei Li,^a Norio Kitadai,^d Samuel M. Webb,^e Takaaki Yano,^f Ryuhei Nakamura,^{id}^{a,g} Masahiko Hara^{a,b} and Shawn E. McGlynn^{id}*^{a,g,h}

Under anaerobic conditions, ferrous iron reacts with sulfide producing FeS, which can then undergo a temperature, redox potential, and pH dependent maturation process resulting in the formation of oxidized mineral phases, such as greigite or pyrite. A greater understanding of this maturation process holds promise for the development of iron-sulfide catalysts, which are known to promote diverse chemical reactions, such as H^+ , CO_2 and NO_3^- reduction processes. Hampering the full realization of the catalytic potential of FeS, however, is an incomplete knowledge of the molecular and redox processes occurring between mineral and nanoparticulate phases. Here, we investigated the chemical properties of iron-sulfide by cyclic voltammetry, Raman and X-ray absorption spectroscopic techniques. Tracing oxidative maturation pathways by varying electrode potential, nanoparticulate $n(\text{Fe}^{2+}\text{S}^{2-})_{(s)}$ was found to oxidize to a Fe^{3+} containing FeS phase at -0.5 V vs. Ag/AgCl (pH = 7). In a subsequent oxidation, polysulfides are proposed to give a material that is composed of Fe^{2+} , Fe^{3+} , S^{2-} and polysulfide (S_n^{2-}) species, with its composition described as $\text{Fe}^{2+}_{1-3x}\text{Fe}^{3+}_{2x}\text{S}^{2-}_{1-y}(\text{S}_n^{2-})_y$. Thermodynamic properties of model compounds calculated by density functional theory indicate that ligand oxidation occurs in conjunction with structural rearrangements, whereas metal oxidation may occur prior to structural rearrangement. These findings together point to the existence of a metastable FeS phase located at the junction of a metal-based oxidation path between FeS and greigite ($\text{Fe}^{2+}\text{Fe}^{3+}_2\text{S}^{2-}_4$) and a ligand-based oxidation path between FeS and pyrite ($\text{Fe}^{2+}(\text{S}_2)^{2-}$).

Received 24th May 2021,
Accepted 23rd July 2021
DOI: 10.1039/d1dt01684a

rsc.li/dalton

^aEarth Life Science Institute, Tokyo Institute of Technology, 2-21-1 IE-1 Ookayama, Meguro, Tokyo 152-8550, Japan. E-mail: sanden@elsi.jp, mcglynn@elsi.jp

^bSchool of Materials and Chemical Technology, Tokyo Institute of Technology, 4259 G1-7 Nagatsuta, Midori-ku, Yokohama, Kanagawa 226-8502, Japan

^cDepartment of Chemistry and Biochemistry, Montana State University, Bozeman, MT 59717, USA. E-mail: szilagy@montana.edu

^dSuper-cutting-edge Grand and Advanced Research (SUGAR) Program, Institute for Extra-cutting edge Science and Technology Avant-garde Research (X-star), Japan Agency for Marine-Earth Science and Technology (JAMSTEC), 2-15 Natsushima-cho, Yokosuka 237-0061, Japan

^eStanford Synchrotron Radiation Lightsource, SLAC National Accelerator Laboratory, 2575 Sand Hill Road, Menlo Park, CA 94025, USA

^fInstitute of Post-LED Photonics, Tokushima University, Minami-Jyosanjima, Tokushima 770-8506, Japan

^gCenter for Sustainable Resource Science, RIKEN, 2-1 Hirosawa, Wako, Saitama 351-0198, Japan

^hBlue Marble Space Institute of Science, Seattle, Washington 98154, USA

†Electronic supplementary information (ESI) available. See DOI: 10.1039/d1dt01684a

Introduction

Iron(II) sulfide is widely encountered in anoxic environments, such as sulfide rich sediments and deep-sea hydrothermal vents.^{1,2} In catalysis research, iron-sulfide minerals are valuable low cost alternatives to those involving precious metals.^{3,4} Stemming from the catalytic ability of iron sulfides to reduce H^+ , CO_2 , and NO_3^- , and the widespread observation of iron-sulfur clusters as catalysts and electron mediators in biology, the mineral phases and their surface chemistry are also of high interest in origin of life studies.^{5–16}

Iron sulfide precipitates undergo a maturation process during which crystallinity, redox state, and molecular stoichiometry may vary.^{17,18} In the most reduced form, $\text{Fe}^{2+}\text{S}^{2-}$ ranges from $n(\text{Fe}^{2+}\text{S}^{2-})_{(aq)}$ colloidal nanoparticles (with $n < 150$) to precipitated iron(II) sulfide ($n > 150$), which we describe as mackinawite-like nanoparticles $n(\text{Fe}^{2+}\text{S}^{2-})_{(s)}$.¹⁹ Below pH 4.5, $n(\text{Fe}^{2+}\text{S}^{2-})_{(aq)}$ also persists as an electroactive, colloidal species with a particle size of ca. 2 nm (referred to as $\text{FeS}_{(nano)}$), which represents an intermediate in the formation of crystalline

mackinawite ($\text{FeS}_{(m)}$) at circumneutral pH.²⁰ The oxidative phase transformations of $\text{Fe}^{2+}\text{S}^{2-}$ to pyrite ($\text{Fe}^{2+}(\text{S}_2)^{2-}$) and greigite ($\text{Fe}^{2+}\text{Fe}^{3+}_2\text{S}^{2-}_4$) are complex; depending on the locus of redox chemistry, the oxidation may be ferrous iron or sulfide ligand centered, forming ferric iron or polysulfides, respectively.¹⁷ The importance of understanding these transitions in catalysis research is highlighted by work showing that a greigite working electrode produced C_2 and C_3 compounds from CO_2 when the potential was cycled between -1 and 0 V vs. Ag/AgCl, but not when a constant potential of -1 V was applied.²¹ From a perspective of Earth history, the FeS maturation sequence and production of polysulfides are relevant to understanding the preservation of biosignatures, through the sulfidization of organic material by substitution reactions with polysulfides and subsequent burial in marine sediments.^{22–24}

Fig. 1 depicts an overview of different mineral phases produced by the oxidation of nanoparticulate or crystalline $\text{FeS}_{(m)}$. Except for the production of pyrite from ferrous iron and polysulfide ions, most reactions are too slow to be readily observed on short experimental time scales at room temperature.^{25,26} When $\text{Fe}^{2+}\text{S}^{2-}$ is oxidized to greigite (Fe_3S_4), marcasite, or pyrite (FeS_2), a two electron oxidation process takes place involving either H_2S or S^0 as an oxidant that favours the oxidation of Fe^{2+} at elevated temperatures (≥ 70 °C) or S^{2-} at room temperature.^{27–29} Furthermore, polysulfides can act as an oxidant for $\text{Fe}^{2+}_{(aq)}$ at elevated temperatures leading to the formation of greigite.³⁰ Moreover, $n(\text{Fe}^{2+}\text{S}^{2-})_{(s)}$ has been implicated to form a soluble iron polysulfide complex or cluster that precipitates slowly as pyrite forms under ambient conditions.^{25,26} To date, only a reaction kinetics model of pyrite formation from $\text{Fe}^{2+}\text{S}^{2-}$ and polarographic data hint the existence of an intermediate in the form of a complex or cluster $[(\text{Fe}-\text{S})_x(\text{S}_n^{2-})_y]$.²⁶

During the oxidation of mackinawite ($\text{FeS}_{(m)}$) to greigite by $\text{Fe}^{3+}_{(aq)}$ or O_2 , a Fe^{3+} containing phase has been detected by Raman and Mössbauer spectroscopy.^{31,32} This FeS phase was

previously undetected likely due to a lack of X-ray diffraction patterns distinguishable from mackinawite owing to poor crystallinity.^{33,34} Based on Mössbauer spectra and Fe K-edge X-ray absorption near-edge structure (XANES) analysis, the Fe^{3+} content of this material was estimated to be up to 20%(mol/mol) of the total iron content and it was termed Fe^{3+} containing mackinawite, with a tentative chemical formula of $\text{Fe}^{2+}_{1-3x}\text{Fe}^{3+}_{2x}\text{S}^{2-}$ ($x < 0.1$).^{33,35} Electrochemical access to this Fe^{3+} containing mackinawite, as well as control over the formation of polysulfides, could allow selective synthesis of pyrite and greigite. Since these minerals promote different reactions, selective synthesis *via* controlled ligand- *versus* metal-based oxidation – as well as access to their intermediates – would be valuable for industrial applications and for understanding the nature of geochemical transformations.

Here, we investigated these oxidative phase transitions by performing cyclic voltammetry on $n(\text{Fe}^{2+}\text{S}^{2-})_{(s)}$, which was freshly precipitated on a solid-state indium tin oxide electrode (ITO). The observed redox reactions suggested from the voltammetric signals were analyzed by *ex situ* sulfur K-edge X-ray absorption near-edge spectroscopy (XANES) and Raman spectroscopy. Computational models for plausible FeS complexes, clusters, and FeS nanoparticles were generated to compare and contrast various compositions and formation mechanisms of Fe^{3+} containing mackinawite.

Experimental section

Iron(II) sulfide was freshly precipitated from an equimolar amount of iron(II) chloride tetrahydrate (99.99%, Sigma) and sodium sulfide nonahydrate (99.99%, Sigma) dissolved in Milli-Q water (18.2 M Ω , Millipore Ltd), which was deaerated by stirring the vial uncapped in a COY glove box overnight prior to usage. All solutions were prepared, and manipulations performed in a plastic sided glove box filled with an atmosphere

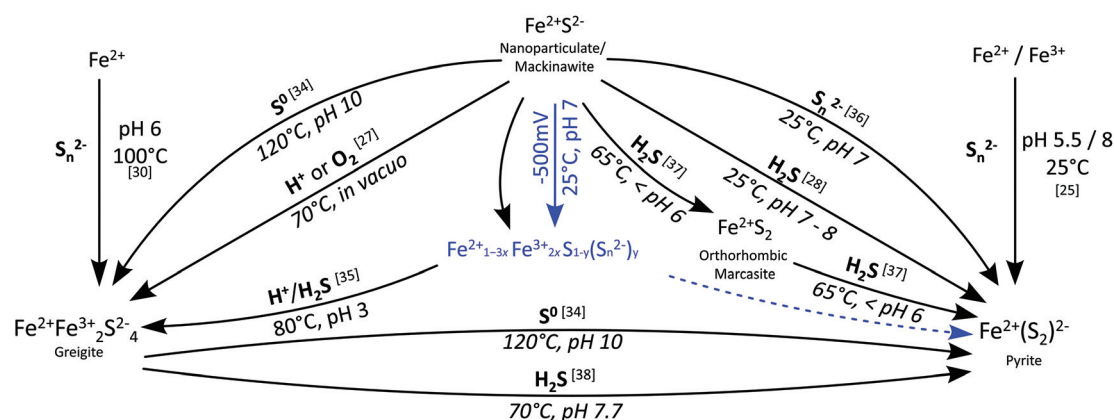


Fig. 1 Schematic overview of the known aqueous oxidation pathways of iron(II) sulfide/mackinawite to greigite, marcasite and pyrite. The oxidants employed or assumed in the respective reaction (and along with literature references) are displayed in bold; the pH and temperature of the reaction conditions are indicated below the oxidants. Indicated in blue is the reaction studied in this work, in which an iron sulfide phase (previously termed ferric iron containing mackinawite³⁵) was produced using an indium tin oxide electrode at -0.5 V vs. Ag/AgCl, pH 7. For a detailed review of mineral transformations of FeS, including higher temperatures, see ref. 17.

of 4% H₂ and 96% N₂ and deoxygenated with palladium catalysts (COY).

The cyclic voltammograms of $n(\text{Fe}^{2+}\text{S}^{2-})_{(s)}$ samples were measured with a HZ-7000 potentiostat (Hokuto Denko) at a scanning speed of 10 mV s⁻¹ and all electrode potentials are given here in reference to Ag/AgCl (in a saturated KCl solution). For these voltammograms, equal volumes (400 μl) of 200 mM FeCl_{2(aq)} and 200 mM Na₂S_(aq) were reacted for 10 min on top of an ITO electrode with a surface area of about 11.3 cm² and then diluted to a 7 ml volume with a K₂HPO₄ buffer solution (200 mM, pH 7.0). For a control experiment containing polysulfides, sodium polysulfides (Na₂S_{*n*}) were first prepared by dissolving 0.7 mmol of Na₂S and adding 2 mmol sublimed elemental sulfur (99%, Wako) in 5 ml Milli-Q water, with heating at 70 °C for 24 h, before being dried *in vacuo* in a 4% H₂/N₂ environment using a dry vacuum pump. As a rough estimate of the molecular weight of Na₂S_{*n*}, the molecular weights of the dominant polysulfide species of Na₂S₂ up to Na₂S₅ were averaged (158 g mol⁻¹).³⁹ 5.7 mM Na₂S_{*n(aq)*} was added to 11.4 mM $n(\text{Fe}^{2+}\text{S}^{2-})_{(s)}$ at an approximate stoichiometric ratio of 2 : 2 : 1 for Fe²⁺ : S²⁻ : S_{*n*}²⁻. For the voltammograms of experiments that did not contain iron, 0.5 mM of Na₂S_(aq) and the prepared Na₂S_{*n(aq)*} (0.5 mM) were dissolved in 100 mM K₂HPO₄ buffer (pH 7) shortly before the analysis as to minimize degassing of H₂S.

For the S K-edge XANES samples, batches of 20 μl of 100 mM FeCl_{2(aq)} and Na₂S_(aq) were reacted first and then diluted with a 100 mM Tris HCl (Sigma) buffer at pH 7.0 to a final volume of 5 ml on top of an indium tin oxide electrode (ITO). An Ag/AgCl electrode in saturated KCl was used as a reference electrode in a conventional triple-electrode assembly and the electrode potential controlled *via* an Ivium Technologies *Compactstat.h* potentiostat. After applying the desired electrode potentials to the samples, the supernatant was removed, and the precipitate was collected by pipet and dried at 60 °C on a hot plate overnight inside the glovebox. As controls for the expected products, 17.6 μmol $n(\text{Fe}^{2+}\text{S}^{2-})_{(s)}$ precipitate was also combined with either 1 mM iron(III) chloride hexahydrate (97%, Sigma) or 1 mM potassium polysulfide (≥42%, Sigma) (molar ratio ~1 : 2.5 Fe²⁺S²⁻ to Fe³⁺ or S_{*n*}²⁻) shortly after precipitation of the material. The dry powders were mounted between a coverslip and a 2 mm × 2 mm and 200 nm thickness silicon nitride window (Norcada) and sealed with a cyanoacrylate-based glue. Samples were sealed in two plastic bags prior to the transfer from the COY glovebox to the beamline.

Sulfur K-edge XANES spectra were recorded at beamline 14-3 of the Stanford Synchrotron Radiation Lightsource (SSRL). The incident X-ray energy was obtained using a Si(111) double crystal monochromator with the Stanford Positron Electron Accelerating Ring (SPEAR) storage ring containing 500 mA at 3.0 GeV in top-off mode. The fluorescence lines of the elements of interest were monitored using a silicon drift Vortex detector (Hitachi) using Xspress3 pulse processing electronics (Quantum Detectors). The sample area was purged with helium gas. Calibration of the X-rays was accomplished

by setting the pre-edge peak of sodium thiosulfate at 2472.02 eV. Suitable spectra from three detector channels were selected using the SIXPACK software package.⁴⁰ The normalization of the spectra was performed using ATHENA.⁴¹

Raman spectra were measured for $n(\text{Fe}^{2+}\text{S}^{2-})_{(s)}$ samples that were prepared as described above for the electrochemical measurements, but with an additional drying step *in vacuo* in order to minimize scattering due to water. The dry powder was placed in an airtight environmental sample cell (LIBcell, Nanophoton) and analyzed by a Raman laser (532 nm) scanning microscope from Nanophoton with a 20× objective in point measurement mode. Each sample was illuminated for 10 s, for which over 200 scattering spectra were collected to generate an averaged spectrum. The spectrum was calibrated against crystalline silicon at 521 cm⁻¹ and the laser power was set to be between 1.5–2.5 mW to ensure that the samples were not exposed to excessive heating during the measurement. The spectra of $n(\text{Fe}^{2+}\text{S}^{2-})_{(s)}$ samples utilized in electrochemical experiments were recorded at a minimum of 3 different locations to assure reproducibility. In this process, only spectra with the same number of peaks and peak positions were averaged; otherwise, they were displayed as individual spectra. As a chemical reference for the possible oxidation products (such as pyrite and greigite), *ca.* 0.5 mmol Na₂S_{*n(aq)*} and 0.1 mmol FeCl_{2(aq)} were reacted in 1 ml Milli-Q water at room temperature for three days prior to analysis.

Density Functional Theory (DFT) calculations were performed using a hybrid, gradient corrected Becke-Perdew86 (BP86) functional with 5% Hartree-Fock exchange in combination with a triple-ζ quality basis set⁴² def2-TZVP as implemented in Gaussian16 Rev.C.01.^{43–45} This functional was selected in order to obtain an experimentally sound description for the electronic and geometric structures of the FeS system. Given the studied aqueous FeS systems and the presence of H₂O after drying of FeS samples, the computational models were embedded in a polarizable solvent continuum (SMD).⁴⁶ The charge distribution was computed using Hirshfeld population analysis method.⁴⁷ Atomic spin density values were obtained from Mulliken population analysis.⁴⁸ Clusters and complexes are noted as ^{*M*}[X]^{*Z*}, where *M* is the spin multiplicity (2*S* + 1) and *Z* the molecular charge of the relevant species X.

Results and discussion

Voltammetry of $n(\text{Fe}^{2+}\text{S}^{2-})_{(s)}$: iron-sulfur redox and the formation of polysulfides

Starting from an open circuit potential of -0.56 V for freshly precipitated $n(\text{Fe}^{2+}\text{S}^{2-})_{(s)}$, the first voltammetric scan was directed toward lower potentials up to -0.80 V (Fig. 2A). The large cathodic current reaching a maximum at -0.80 V was observed in all voltammetric experiments and is attributed to proton reduction producing H₂. The first anodic peak (A1) was observed at -0.39 V (Fig. 2A), a smaller second peak at -0.19 V (A2), and a third at -0.05 V (A3).

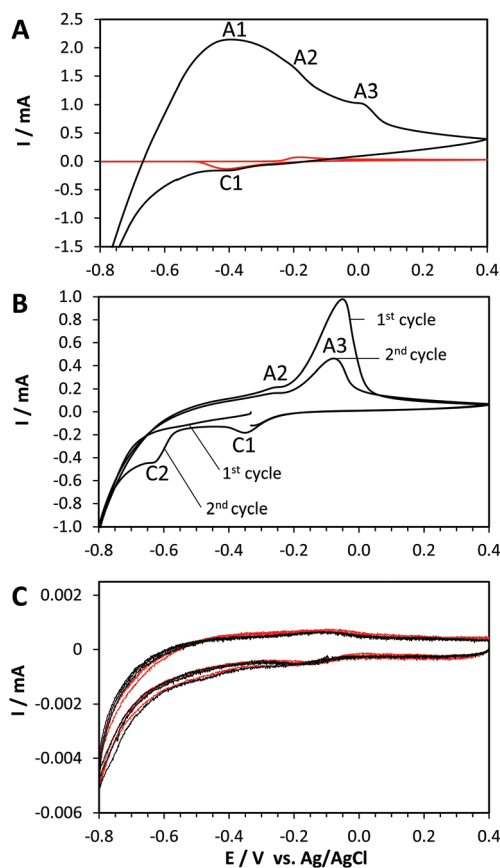
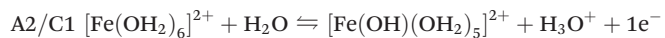


Fig. 2 Cyclic voltammograms of (a) the first cycle of $n(\text{Fe}^{2+}\text{S}_n^{2-})_{(s)}$ (formed from equimolar 11.4 mM $\text{Fe}^{2+}_{(aq)}$ and $\text{S}_n^{2-}_{(aq)}$) shown by the black trace and 11.4 mM FeCl_3 only by the red trace (for which the second voltammetric cycle is shown). (b) 5.7 mM $\text{Na}_2\text{S}_{n(aq)}$ and $n(\text{Fe}^{2+}\text{S}_n^{2-})_{(s)}$ (formed as above) in 200 mM K_2HPO_4 (pH 7), which shows both the first and second voltammetric cycle. Panel (c) depicts a voltammetric sweep of 0.5 mM $\text{Na}_2\text{S}_{(aq)}$ (red) and ca. 0.5 mM $\text{Na}_2\text{S}_{n(aq)}$ in a 100 mM K_2HPO_4 buffer (pH 7) (black). The scanning speed was 10 mV s^{-1} and the open circuit potential was the starting point for the potential sweep.

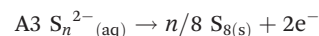
Similar to A2, $\text{FeCl}_{3(aq)}$ in a 200 mM K_2HPO_4 pH 7 buffer showed a redox wave with an anodic peak at -0.18 V (Fig. 2A, red trace). Additionally, the cathodic sweep showed a peak for both $n(\text{Fe}^{2+}\text{S}_n^{2-})_{(s)}$ and $\text{FeCl}_{3(aq)}$ at -0.41 V (C1). Since $[\text{Fe}(\text{OH})_2]^{2+}_{(aq)}$ co-exists with $n(\text{Fe}^{2+}\text{S}_n^{2-})_{(s)}$ despite $\text{FeCl}_{2(aq)}$ and $\text{Na}_2\text{S}_{(aq)}$ being reacted in 1 : 1 stoichiometries (in 11.4 mM concentration),⁴⁹ A2 and C1 are attributed to the reversible redox reaction of aqueous $\text{Fe}^{2+}/\text{Fe}^{3+}$ at pH 7:



Adding S_n^{2-} to $n(\text{FeS})_{(s)}$ in a 1 : 2 stoichiometric ratio significantly changed the voltammogram. The current for peak A1 decreased (Fig. 2B), which coincided with the precipitate becoming a black suspension. Solubilization of $n(\text{Fe}^{2+}\text{S}_n^{2-})_{(s)}$ was observed previously with polysulfide addition at pH 7. $[\text{Fe-S}]_x(\text{S}_n^{2-})_y$ complexes or clusters were proposed to be the reaction product exhibiting an anodic peak.²⁵ Contrary to this, in our samples, no new anodic peak was observed. A decreased

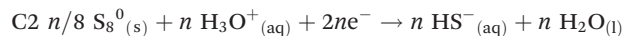
current for A1 might be attributed to diminished contact with the electrode upon solubilization of $n(\text{Fe}^{2+}\text{S}_n^{2-})_{(s)}$ or could also be attributed to a decreased electroactivity due to the presence of a high concentration of negative charged polysulfide species interfering with electronic contact with the ITO electrode.

The addition of S_n^{2-} led to peak A3 exhibiting the highest anodic current at about -0.05 V (Fig. 2B). This reaction is proposed to be the oxidation of polysulfides to elemental sulfur according to the following reaction:



Based on the free energies of formation for polysulfides³⁹ and rhombic elemental sulfur⁵⁰ in aqueous solution, the oxidation of the most abundant (deprotonated) $\text{S}_5^{2-}_{(aq)}$ species has a standard reduction potential of -0.54 V vs. Ag/AgCl, but an oxidation potential of ~ 0 V (pH 6.8) similar to peak A3 was reported for polysulfide oxidation on Au electrodes.⁵¹

After an anodic scan, another cathodic peak (C2) appeared at -0.63 V for $n(\text{Fe}^{2+}\text{S}_n^{2-})_{(s)}$ in the presence of $\text{S}_n^{2-}_{(aq)}$ (Fig. 2B). The standard reduction potentials of the S_8/HS^- and the $\text{S}_2^{2-}/\text{HS}^-$ redox pairs are -0.34 V and -0.32 V Ag/AgCl (pH 7) respectively.³² As peak C2 is only observed on the second scan, after the putative deposition of elemental sulfur at peak A3, the reduction of S_8 likely proceeds as:



Importantly, no oxidation reaction occurs on the ITO electrode using solely $\text{Na}_2\text{S}_{(aq)}$ or $\text{Na}_2\text{S}_{n(aq)}$ in a phosphate buffer (Fig. 2C). Thus, none of the above assigned peaks for $n(\text{Fe}^{2+}\text{S}_n^{2-})_{(s)}$ with or without polysulfides can be attributed to the underpotential deposition of sulfide on the electrode surface, as reported for Au electrodes.⁵¹ The suppression of sulfide oxidation on ITO has been reported earlier when a phosphate buffer was used. It was hypothesized that $\text{H}_2\text{PO}_4^-/\text{HPO}_4^{2-}$ anions hinder the diffusion of $\text{HS}^-_{(aq)}$ to the electrode surface.⁵² This demonstrates that the presence of iron ions is necessary to render sulfide and polysulfides electroactive on ITO in a 100 mM phosphate buffer, and suggests that the oxidation of iron-bound sulfides to polysulfides might also feature metal-centered redox changes.

XANES spectroscopy: iron oxidation precedes sulfur oxidation

To gain more insight into the iron and sulfur redox changes occurring on the electrode, XANES spectroscopic measurements were performed with samples oxidized at electrode potentials corresponding to the observed anodic peaks. Trace (a) in Fig. 3 depicts the S K-edge XANES spectrum of untreated $n(\text{Fe}^{2+}\text{S}_n^{2-})_{(s)}$ with its main edge peak located at 2471.0 eV. To obtain samples of $n(\text{FeS})_{(s)}$ that incorporate Fe^{3+} and S_n^{2-} ions, either $\text{Na}_2\text{S}_{n(aq)}$ or $\text{FeCl}_{3(aq)}$ were added to $n(\text{Fe}^{2+}\text{S}_n^{2-})_{(s)}$ in a molar ratio 1 : 2.5 $\text{Fe}^{2+}\text{S}_n^{2-}$ to Fe^{3+} or S_n^{2-} (trace (b) and (d)). Fig. 3, trace (c) displays the S K-edge absorbance of $n(\text{Fe}^{2+}\text{S}_n^{2-})_{(s)}$, which was cycled between -0.5 V and -0.2 V for 3.5 h to accumulate polysulfides between the potentials of their oxidation to sulfur (peak A3) and the onset of the large cathodic current at -0.5 V. Both the control experiment of

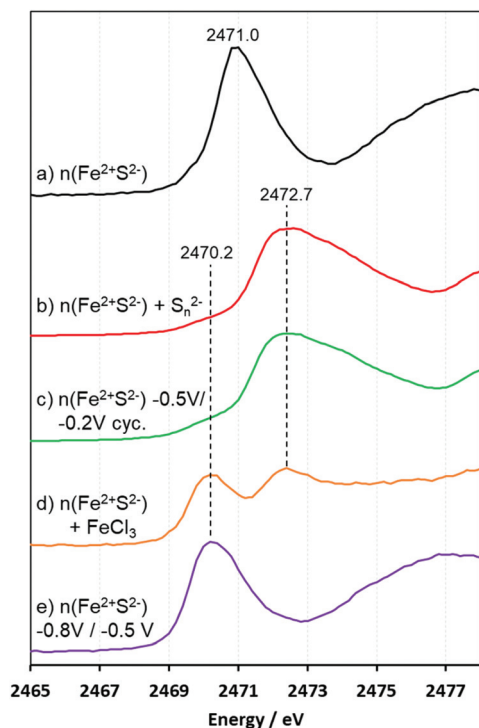


Fig. 3 Normalized sulfur K-edge X-ray near-edge absorbance spectra of untreated $n(\text{Fe}^{2+}\text{S}^{2-})_{(\text{s})}$ (a), $n(\text{Fe}^{2+}\text{S}^{2-})_{(\text{s})}$ to which $\text{Na}_2\text{S}_{n(\text{aq})}$ was added (b) and $n(\text{Fe}^{2+}\text{S}^{2-})_{(\text{s})}$ cycled between -0.5 V and -0.2 V (c). Samples for $n(\text{Fe}^{2+}\text{S}^{2-})_{(\text{s})}$ incorporating Fe^{3+} were obtained by the addition of FeCl_3 to $n(\text{Fe}^{2+}\text{S}^{2-})_{(\text{s})}$, depicted in trace (d), or electrochemical oxidation of $n(\text{Fe}^{2+}\text{S}^{2-})_{(\text{s})}$ at -0.5 V (e). The energy scale is expressed in electron volts and was calibrated against the first pre-edge feature of sodium thiosulfate at 2472.02 eV.

$n(\text{Fe}^{2+}\text{S}^{2-})_{(\text{s})}$ with added $\text{S}_{n^{2-}}(\text{aq})$ (Fig. 3, trace (b)) and the electrochemical experiment (Fig. 3, trace (c)) show the main edge peak at 2472.7 eV, which is also observed for $\text{S}_{8(\text{s})}$ (ESI, Fig. S1,† trace (i)).

The weak and broad pre-edge feature at 2470.2 eV may correspond to the presence of small amounts of polysulfides, as these features arise from the 1s to 3p -based, S-S σ^* transitions of the terminal and internal sulfur atoms at 2472.7 eV, respectively.⁵³ However, these pre-edge features can also arise from alternative species, such as S-radicals, cation bound terminal S atoms of persulfides (*i.e.* vacant Li $2\text{s}/2\text{p}$ mixing with occupied S 3p orbitals)⁵⁴ or covalent Fe-S bonding (vacant Fe 3d mixing with occupied S 3p orbitals).⁵⁵ The main transition at 2472.7 eV and the pre-edge feature at 2470.2 eV could thus correspond to either polysulfides or elemental sulfur and covalent $\text{Fe}^{3+}\text{-S}^{2-}$ bonds.

To determine the changes of the electronic environment and redox state of sulfide at voltametric peak A1, $n(\text{Fe}^{2+}\text{S}^{2-})_{(\text{s})}$ was exposed to -0.8 V for 1.5 h (following the scan direction of the voltametric experiments) and then stabilized at -0.5 V for 2 h (Fig. 3, trace (e)). The main edge of the electrochemical experiment at 2470.2 eV coincides with the Fe^{3+} containing $n(\text{Fe}^{2+}\text{S}^{2-})_{(\text{s})}$ control sample (Fig. 3, trace (d)), whereas the

sulfur K-edge peak of untreated $n(\text{Fe}^{2+}\text{S}^{2-})_{(\text{s})}$ can be found 0.8 eV higher (Fig. 3, trace (a)). The pre-edge feature shift to lower energies for Fe^{3+} bound sulfides is due to the higher nuclear charge of ferric iron that lowers the Fe d-manifold relative to ferrous iron, as was demonstrated by the S K-edge XANES spectra of metal thiolate complexes and $[\text{4Fe-4S}]$ clusters.^{55,56} The anodic current A1 can thus be associated with the oxidation of $n(\text{Fe}^{2+}\text{S}^{2-})_{(\text{s})}$ to a ferric iron bound to sulfide, although quantification is prohibited since both the rising-edge feature of terminal polysulfides and pre-edge ferric sulfide show a peak at 2470.2 eV.⁵⁴ The absence of a signal corresponding to S_8^0 at around 2472.7 eV after applying -0.5 V to $n(\text{Fe}^{2+}\text{S}^{2-})_{(\text{s})}$ suggests that the oxidation of iron precedes the oxidation of sulfide.

Raman spectroscopy: an oxidative progression to ferric iron containing mackinawite

Raman spectra for $n(\text{Fe}^{2+}\text{S}^{2-})_{(\text{s})}$ were measured after applying a potential of -0.8 V, -0.35 V, or 0 V for 48 h (Fig. 4, traces (a)–(c)). The sample exposed to 0 V was also reanalyzed after 2 months storage inside a glovebox maintaining an O_2 level of below the detection limit (≤ 20 ppm). From the -0.8 V preparation, the $n(\text{Fe}^{2+}\text{S}^{2-})_{(\text{s})}$ precipitate exhibited the characteristic vibrational modes of mackinawite at 207 cm^{-1} ($a_{1\text{g}}$ mode) and

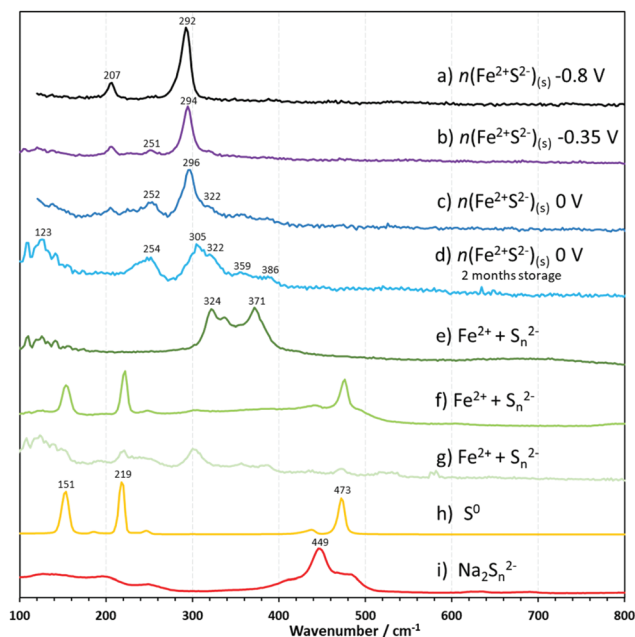


Fig. 4 Raman spectra of electrochemically treated $n(\text{Fe}^{2+}\text{S}^{2-})_{(\text{s})}$, a reaction between ferrous iron and polysulfides, and reference materials. Spectra (a) to (c) depict $n(\text{Fe}^{2+}\text{S}^{2-})_{(\text{s})}$ with applied potentials of -0.8 V (a), -0.35 V (b), 0 V (c) and $n(\text{Fe}^{2+}\text{S}^{2-})_{(\text{s})}$ to which an electrode potential of 0 V vs. Ag/AgCl was applied and subsequently stored in an anaerobic environment 2 months prior to the analysis (d). Dry, heterogeneous material obtained from a reaction of FeCl_2 and $\text{Na}_2\text{S}_{n(\text{aq})}$ is depicted in (e), (f) and (g) sublimed elemental sulfur in (h) and a preparation of $\text{Na}_2\text{S}_{(\text{s})}$ under anaerobic conditions is displayed in (i). The Raman peak positions for the electrochemical experiments are presented in Fig. S2 (ESI).†

292 cm^{-1} (b_{1g} mode) (Fig. 4, trace (a)).^{35,57} Exposure to a potential of -0.35 V produced new Raman bands at 251 cm^{-1} and at 322 cm^{-1} (Fig. 4, trace (b)), which were both previously assigned to Fe^{3+} containing mackinawite.^{32,35}

The spectra acquired at 0 V for the freshly precipitated and aged $n(\text{Fe}^{2+}\text{S}^{2-})_{(s)}$ display broad peaks that are distinct from mackinawite at ~ 253 , 322, and 350–360 cm^{-1} (Fig. 4, traces (c) and (d)). These peaks are consistent with the previously reported Raman bands for Fe^{3+} containing mackinawite.³⁵ The Raman band at 359 cm^{-1} detected for aged $n(\text{Fe}^{2+}\text{S}^{2-})_{(s)}$ at 0 V could also correspond to the highest intensity Raman bands of greigite at ~ 355 and ~ 365 cm^{-1} , but other vibrational modes (190 and 247 cm^{-1}) of this mineral were not observed. The appearance of the additional Raman band at 359 cm^{-1} , as well as an increase in peak intensities (relative to the b_{1g} mode of mackinawite near 295 cm^{-1}) suggests an oxidative progression from -0.35 V to 0 V. The $n(\text{Fe}^{2+}\text{S}^{2-})_{(s)}$ b_{1g} normal mode shifted from 292 cm^{-1} at -0.8 V to 297 cm^{-1} at 0 V, and up to 305 cm^{-1} after 2 months storage under anaerobic conditions. This blue shift of the normal mode was previously attributed to the presence of ferric iron³⁵ and is also consistent with an oxidative progression at more positive electrode potentials. This interpretation that the shift of the ~ 295 cm^{-1} feature is related to the presence of Fe^{3+} ion, is affirmed here based on the example of oxidized $[\text{8Fe-8S}]$ cluster models derived from DFT, which are discussed below (cf. Fig. 5 and 6).

As the oxidation of sulfide to form polysulfides was suggested to occur in $n(\text{Fe}^{2+}\text{S}^{2-})_{(s)}$ during our cyclic voltammetry experiments (as evinced by polysulfide oxidation at A3 of Fig. 2A and B), a complementary reference material was prepared by reacting $\text{Na}_2\text{S}_{n(\text{aq})}$ with $\text{FeCl}_{2(\text{aq})}$. This experiment was found to give a heterogeneous material, of which three representative spectra are shown in Fig. 4, traces (e)–(g). Spectrum (e) shows peaks characteristic for pyrite at 324 and 374 cm^{-1} and also an additional peak at 337 cm^{-1} of unknown origin. The Raman spectrum of elemental sulfur (Fig. 4, trace (h)) displays peaks at 151, 219, and 473 cm^{-1} , which can also be found as minor peaks in spectrum (g) in Fig. 4. This indicates the formation of elemental sulfur upon addition of polysulfides to ferrous iron. The high intensity peak at 302 cm^{-1} in spectrum (g) is assumed to originate from $n(\text{Fe}^{2+}\text{S}^{2-})_{(s)}$, which, together with the presence of elemental sulfur, matches earlier findings that the first products formed during the reaction of $\text{S}_n^{2-}(\text{aq})$ and $\text{Fe}^{2+}(\text{aq})$ are $n(\text{Fe}^{2+}\text{S}^{2-})_{(s)}$ and $\text{S}^0_{(s)}$.¹⁷ Neither the $\text{Fe}^{2+} + \text{S}_n^{2-}$ reference material nor electrochemically oxidized $n(\text{Fe}^{2+}\text{S}^{2-})_{(s)}$ exhibit the highest intensity Raman band at 449 cm^{-1} found for $\text{Na}_2\text{S}_{n(s)}$ (Fig. 4i), which suggests the absence of non-coordinated, long chain polysulfides in our samples. Spectra (d), (e) and (g) in Fig. 4 exhibit the same closely spaced peaks at 94, 110, 119, 126, 134 and 143 cm^{-1} for both the electrochemical experiment at 0 V and the reaction of $\text{Fe}^{2+} + \text{S}_n^{2-}$. These features are proposed here to arise from the coordination of polysulfide species to Fe^{2+} and Fe^{3+} , as dis-

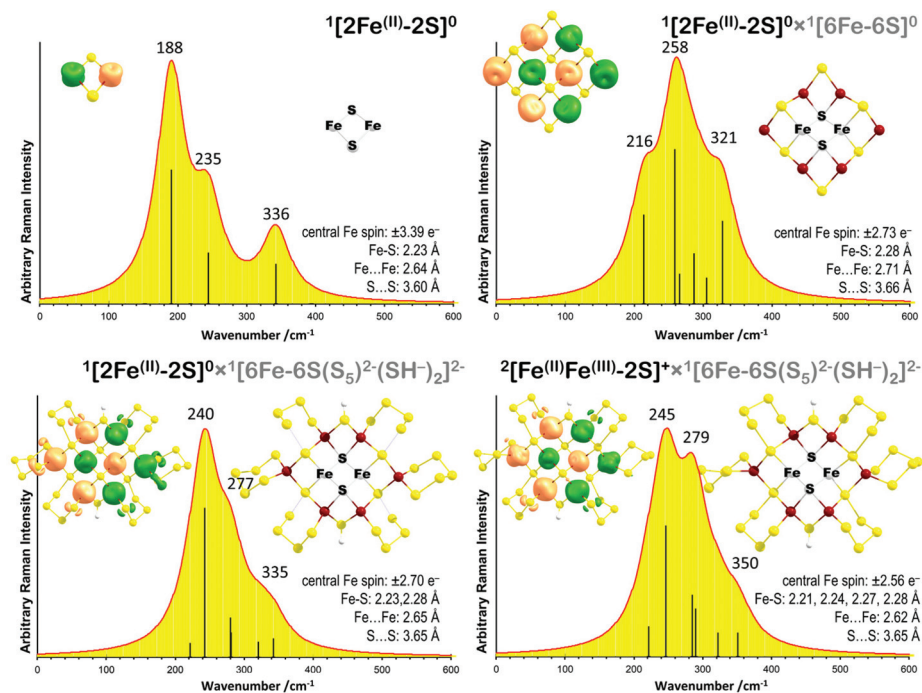


Fig. 5 Simulated Raman spectra for the $1[2\text{Fe}-2\text{S}]^0$ rhomb (top left), the $1[8\text{Fe}-8\text{S}]^0$ cluster or core $1[2\text{Fe}-2\text{S}]^0$ rhombs embedded in a ring of $1[6\text{Fe}-6\text{S}]^0$ as a model for $8(\text{FeS})_{(\text{aq})}$ nanoparticles (top right), and the persulfide and bisulfide terminated $8(\text{FeS})_{(\text{aq})}$ nanoparticle model in an all ferrous (bottom left) and one-electron oxidized form (bottom right) with selected intramolecular distances at B(5%HF)P86/def2TZP/SMD(water) level of theory. Interatomic distances, atomic spin densities, and spin density contour plots (orange/green are positive and negative spin contours at $0.01 \text{ e}^{-2} \text{ \AA}^{-3}$ levels), are provided to illustrate the electronic and geometric structural differences among the models.

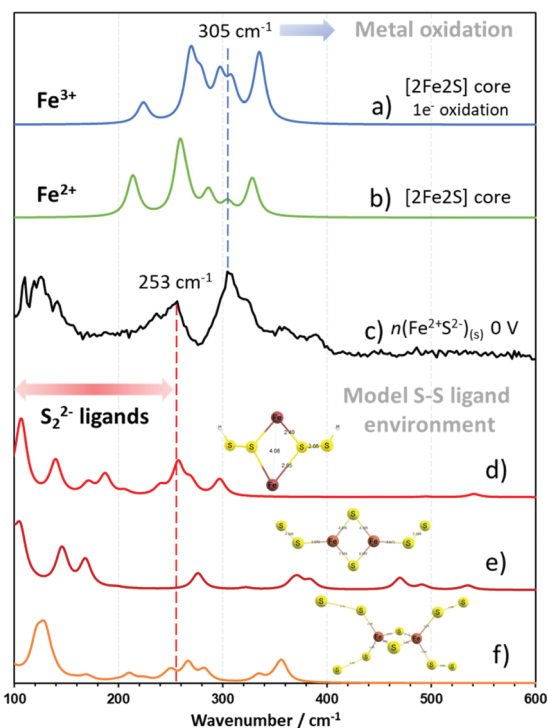


Fig. 6 Simulated Raman spectra of [2Fe-2S] cores from FeS nanoparticles and model persulfide ligand environments on the example of [2Fe-2S] clusters, in comparison to $n(\text{Fe}^{2+}\text{S}^{2-})_{(s)}$ oxidized at 0 V. Spectra (a) and (b) correspond to core extracted [2Fe-2S] rhombs, where (a) depicts the blue-shifted Raman bands of a $1e^-$ oxidized $8(\text{FeS})_{(aq)}$ particle and (b) the non-oxidized, neutral charge $8(\text{FeS})_{(aq)}$ particle. Raman spectrum (c) depicts the measured spectrum of $n(\text{Fe}^{2+}\text{S}^{2-})_{(s)}$ oxidized at 0 V, which was stored anaerobically for 2 months. Spectra (d) to (f) show the vibrational modes of persulfide ligated [2Fe-2S] clusters, where (d) corresponds to ${}^2[\text{2Fe}-(\text{SSH})_2]^{3+}$, (e) to ${}^1\{[\text{2Fe}-2\text{S}](\text{S}_2^{2-})_2\}^{4-}$ and (f) to ${}^1\{[\text{2Fe}-2\text{S}](\text{S}_2^{2-})_4\}^{8-}$.

cussed below for the computed resonance frequencies of metal bound persulfides and polysulfides.

Vibrational analysis of $n(\text{Fe}^{2+}\text{S}^{2-})_{(aq)}$ nanoparticle models ($n = 8$)

The origin of the observed changes in the Raman peak positions during electrochemical oxidation was investigated by using DFT-based vibrational analyses. The literature often cites the [2Fe-2S] rhomb as the characteristic structural unit of mackinawite, which is only correct when considering stoichiometry.¹⁷ In order to correlate spectral and electrochemical features to composition and structure, we first modelled the metal- and ligand-based redox changes of an isolated [2Fe-2S] rhomb. The changes in the Fe-S bonding and consequences to the Raman active vibrational modes are summarized in Table S1 (ESI)[†] and discussed in the ESI Appendix.[†]

Building on these computational models, we derived [2Fe-2S] core-only Raman active modes to eliminate the interfering peaks from peripheral dangling groups encountered when the [2Fe-2S] unit is part of a larger molecule. This focus on the core is warranted because the contribution of dangling groups

to the experimentally observed Raman peaks is negligible due to their low surface concentrations relative to the bulk of the nanoparticle surface. At the same time, the polarizable continuum embedded [8Fe-8S] cluster is a realistic, experimentally relevant species for mackinawite-like nanoparticle formation in the smaller nucleation domain.¹⁹ The [8Fe-8S] cluster is the smallest model which can compose a chemically reasonable representation of a central [2Fe-2S] rhomb embedded in a ring of peripheral 6Fe^{2+} and 6S^{2-} ions, where termination of the [2Fe-2S] rhomb environment completes the tetrahedral and tetragonal pyramidal coordination for the ferrous and sulfide ions, respectively. The core-extracted Raman spectra validate the accuracy of the employed level of theory in predicting Raman spectra by a scaled-quantum mechanical force field (SQM-FF) treatment (see Table S2, ESI)[†].^{58,59} Using the experimental Raman peaks of mackinawite, a periodic computational model,⁶⁰ and our molecular cluster model, we obtain a 94-96% scaling factor and 11-16 cm^{-1} shift to achieve the best least-square fit to experiment. The SQM-FF parameters cause non-significant changes in the calculated spectra in comparison to our experimentally observed chemical shifts; thus, we did not employ them in our current study.

Fig. 5 compares these peripheral chemical environments from the complete absence in [2Fe-2S], through an incomplete [8Fe-8S] model without polysulfides, to a plausible persulfide saturated limit for the formally all ferrous and mixed ferrous/ferric central [2Fe-2S] rhombs. With the exception of the isolated [2Fe-2S] rhomb, the dominance of a 240-280 cm^{-1} feature is apparent (Fig. 5). Structural and electronic perturbations are manifested in the variation of the peak intensity, line-shape, and slight shift of envelop of Raman peaks around 250 cm^{-1} , which is thought to correspond to the first distinct Raman band at $\sim 253 \text{ cm}^{-1}$ observed during the oxidation of $n(\text{Fe}^{2+}\text{S}^{2-})_{(s)}$ (Fig. 4, traces (b)-(d)). A $1e^-$ oxidation of the [8Fe-8S] neutral cluster results in a small shift of the Raman peaks to higher wavenumbers as compared to the [2Fe-2S] clusters given that the electron hole delocalizes throughout the entire cluster (see [8Fe-8S]^{0/+} in Table S1, (ESI).[†] Importantly, this shift matches the observations that higher applied oxidation potentials cause a shift of the normal mode of $n(\text{Fe}^{2+}\text{S}^{2-})_{(s)}$ from 294 to 305 cm^{-1} (Fig. 4, traces (a)-(d)). With these results, we propose that the experimentally observed intensity increase of the $\sim 253 \text{ cm}^{-1}$ peak is originating from the presence of molecular ferrous iron/sulfide clusters with defects, due to oxidation state change (to nominally ferric iron), or variation in the ligand environment (persulfide, polysulfide, bisulfide versus bridging sulfides). This peak was predicted to be present for the idealized mackinawite periodic structure only at a very low intensity, which may become more prominent due to lattice defects induced by oxidation.⁵⁷

Persulfide and polysulfide ligand environment

In addition to the core-extracted [2Fe-2S] rhombs, smaller [2Fe-2S] clusters with persulfide ligands were also computed to investigate the vibrational modes of iron bound persulfides. FeS clusters with bridging persulfides or terminal persulfide

ligands produce several high intensity Raman bands below 253 cm^{-1} , similar to the observed Raman bands in the electrochemical experiments (Fig. 6, traces (c)–(f)). The $^2[\text{2Fe}-(\text{SSH})_2]^{3+}$ cluster also exhibits a vibrational mode at 257 cm^{-1} (Fig. 6, trace (d)), which is close to the 253 cm^{-1} peak observed for $n(\text{Fe}^{2+}\text{S}^{2-})_{(s)}$ at 0 V. The high intensity vibrational modes below 140 cm^{-1} and near 253 cm^{-1} were also calculated for hypothetical iron persulfide complexes, which are intended to serve as a model ligand environment for iron bound persulfides (Fig. S32–S57, ESI†). Based on these observations, the closely spaced Raman peaks below 140 cm^{-1} in the experimental spectra (Fig. 4, traces (d), (e), and (g)), could therefore originate from iron bound persulfides.

The increase in the relative Raman intensities below 140 cm^{-1} for $n(\text{Fe}^{2+}\text{S}^{2-})_{(s)}$ from -0.8 V to 0 V (Fig. 4) and this analysis corroborates the interpretation of the cyclic voltammetry experiments that polysulfides, and disulfides in particular, are generated through the oxidation of sulfide above -0.5 V .

The synthesis and structural characterization of a $[\text{2Fe}-(\text{2S})]$ cluster with two pentasulfide ligands has been reported.⁶¹ The calculated equilibrium structure at the employed level of theory is in good agreement with the measured structure and has a root mean square deviation in bond lengths and bond angles of 0.02 \AA and 0.9° , respectively. The vibrational normal modes were calculated and highly Raman active polysulfide stretching modes above 400 cm^{-1} were observed for the nominally ferrous iron containing $^1\{[\text{2Fe}^{2+}-(\text{2S})](\text{S}_5^{2-})_2\}^{4-}$ (Fig. S13, ESI†). The measured Raman spectrum of $\text{Na}_2\text{S}_{n(s)}$ exhibits similar high intensity Raman band at 449 cm^{-1} (Fig. 4e), corresponding to internal S–S stretching modes of polysulfides.⁶² Because no Raman bands were observed $>400\text{ cm}^{-1}$ in any of the studied electrode potentials, pentasulfide clusters and non-iron bound polysulfides appear to be a less likely reaction product than iron coordinated persulfide species, which produce high intensity Raman bands below 253 cm^{-1} . The voltametric peaks A3 and C2 (Fig. 2) could thus be mainly associated with disulfide species, although the equilibrium between the different chain lengths of polysulfides might have been altered during drying of the samples.

Thermodynamics of metal and ligand-based oxidation

Based on our results that indicate initial formation of a ferric phase during FeS oxidation (Fig. 1), we composed a potential energy surface of electronically varied, but stoichiometrically equivalent FeS models (Fig. 7A). These models connect the postulated metal- and ligand-based intermediates and allow an initial assessment of possible states which may precede iron loss or sulfur addition during $n(\text{Fe}^{2+}\text{S}^{2-})_{(aq)}$ nanoparticle oxidation. The reference structure is the neutral $[\text{2Fe}-(\text{2S})]$ rhomb with antiferromagnetically coupled $S = 2$ iron centers; a transient species formed during nucleation of mackinawite-like $n(\text{Fe}^{2+}\text{S}^{2-})_{(aq)}$ nanoparticles.¹⁷ The $[\text{2Fe}-(\text{2S})]$ reference state can be represented by the $(\text{Fe } 3d^{6+6}/\text{S } 3p^{8+8})$ electron configuration. Upon $1e^-$ oxidation (bottom red arrow in Fig. 7A), the rhomb converts to a mixed valence ferrous/ferric $[\text{2Fe}-(\text{2S})]^+$ paramagnetic ($S_t = 1/2$) state. The oxidation step is spon-

taneous by -12 kJ mol^{-1} ($E^\circ = +130\text{ mV vs. Ag/AgCl}$). The second oxidation forms the diferric rhomb in a now endergonic step by 72 kJ mol^{-1} ($E^\circ = -308\text{ mV}$). The $2e^-$ oxidized rhomb's electron configuration is $(\text{Fe } 3d^{5+5}/\text{S } 3p^{8+8})$, corresponding to metal-based oxidation. The latter two rhombs are the physiologically relevant forms of plant ferredoxins with comparable midpoint potentials (-340 to -500 mV).^{63–65} The stability of protein bound diferric rhombs is due to the strong terminal L(thiolate)–M bond, which was not considered here for the sake of preserving the stoichiometry of intermediates throughout the entire potential energy surface.

Ligand-based oxidation cannot be directly accessed from the neutral, diamagnetic rhomb $[\text{2Fe}-(\text{2S})]$. Instead, we constructed the chain model of a diferrous persulfide complex, $[\text{Fe}-(\text{SS})-\text{Fe}]^{2+}$ *trans* isomer shown in the bottom left of Fig. 7A, which corresponds to the electron configuration of $(\text{Fe } 3d^{6+6}/\text{S } 3p^{7+7})$. Unexpectedly, this pyrite mimic, without a ligand environment around the terminal ferrous centers and the persulfide anion, is only 35 kJ mol^{-1} ($E^\circ = -179\text{ mV}$) higher than the reference $[\text{2Fe}-(\text{2S})]$ rhomb. The $1e^-$ reduction of the *trans* isomer (top blue arrow) leads to ligand-based redox changes, where the persulfide bond order is reduced and the S–S bond length in S_2^{3-} is elongated by 0.2 \AA relative to S_2^{2-} . The paramagnetic $[\text{Fe}-(\text{SS})-\text{Fe}]^+$ *trans* species is unstable ($+142\text{ kJ mol}^{-1}$ and $E^\circ = -1.471\text{ V}$) without the presence of a ligand environment around the terminal Fe^{2+} ions. An additional reduction step leads to complete dissociation and formation of two weakly interacting FeS diatomic molecules. These two FeS units can condense to form the initially discussed, neutral $[\text{2Fe}-(\text{2S})]$ rhomb. In line with this pathway, literature examples showed that, during reductive dissolution of pyrite, the FeS unit containing mineral pyrrhotite ($\text{Fe}_{(1-x)}\text{S}$), where $x < 0.17$) is formed.⁶⁶

In order to further explore the energy landscape and transitions between the pyrite mimic and mackinawite rhomb, including changes in the metal and ligand oxidation states, a plausible set of intermediates were generated by morphing the $[\text{2Fe}-(\text{2S})]$ rhomb and the $[\text{Fe}-(\text{SS})-\text{Fe}]^{2+}$ chain. The morphing is along a coupled vibrational coordinate, where the two ferrous centers stretch in sync with the contraction of the S...S distance. The rhomb-to-chain morphing resulted in three unique intermediate structures, which are a lower energy $[\text{FeSFeS}]^+$ chain isomer, a $[\text{FeSSFe}]^+$ chain *cis* isomer, and a dissociated $[\text{FeS}] + [\text{FeS}]^+$ pair of diatomic molecules. The reverse, chain-to-rhomb morphing resulted only in two intermediates, which is a lower energy $[\text{Fe}-(\text{SS})-\text{Fe}]^+$ *cis* isomer that is identical to the one found along the first morphing path ($[\text{FeSSFe}]^+$ chain *cis* isomer). The other isomer is very similar to the aforementioned $[\text{FeS}] + [\text{FeS}]^+$ pair. Thus, the energetic degeneracy of the $[\text{Fe}-(\text{SS})-\text{Fe}]^+$ *cis* isomer and the $[\text{FeS}] + [\text{FeS}]^+$ pair offer a transition path between the metal- and ligand-based redox processes.

With the key isomers identified, we draw a potential pathway for connecting the metal- (Fig. 7A right-hand side) and ligand (Fig. 7A left-hand side) based redox chemistry and show this in Fig. 7B. Starting from freshly precipitated $n(\text{Fe}^{2+}\text{S}^{2-})_{(s)}$, a one electron electrochemical oxidation results

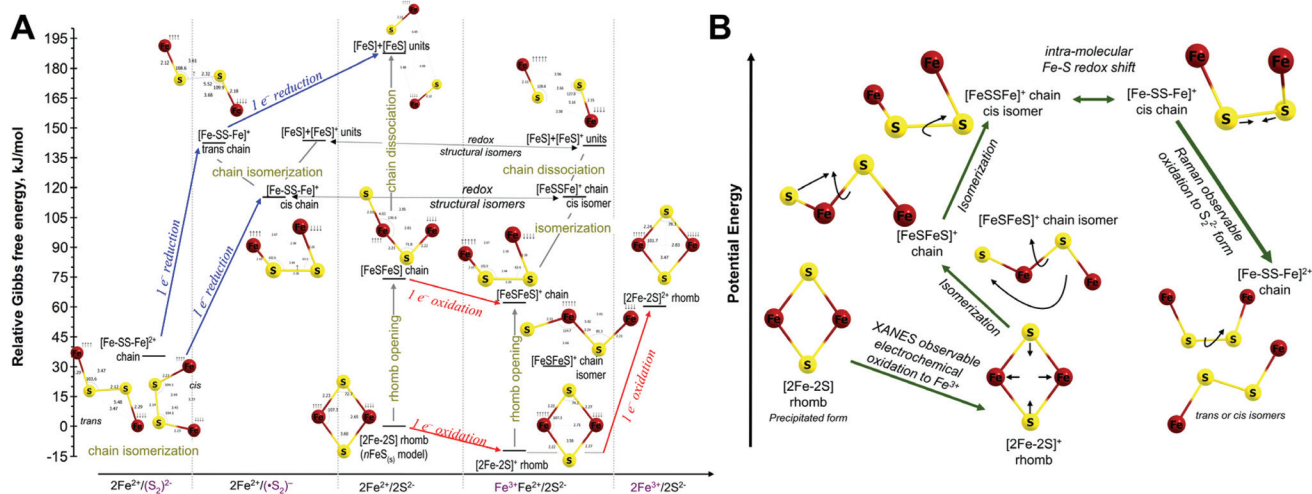


Fig. 7 (A) Potential energy surface map of redox processes between the mackinawite-like $[2\text{Fe}-2\text{S}]$ rhomb (bottom right) and a pyrite-like $[\text{Fe}-\text{SS}-\text{Fe}]^{2+}$ ligand oxidized chain (bottom left) with conserved stoichiometry. Blue and red arrows indicate $1e^-$ reduction and oxidation steps, respectively. Changes in the oxidation state of Fe and S within the models are indicated on the x-axis. Thin, olive green vertical lines mark changes in chemical bonding for isoelectronic, isomeric species with the same metal and ligand redox state. Small black arrows correspond to the number and spin of unpaired electrons. Gibbs energies were estimated at B(5%HF)P86/def2TZVP/PCM (water SMD) level of theory. The electron energy for redox is taken from Ag/AgCl potential +197 mV relative to SHE (4.21 V). (B) The FeS transitions that are directly relevant to the cyclic voltammetry presented here are shown, illustrating a potential pathway between precipitated FeS and pyrite. Precipitated $n(\text{Fe}^{2+}\text{S}^{2-})_{(s)}$ (modeled as a $2(\text{FeS})_{(aq)}$ rhomb) is electrochemically oxidized, producing a ferric iron containing species observed by XANES. A pathway of isomerizations leads to an intra-molecular redox shift where 2Fe^{3+} oxidizes 2S^{2-} to $(\text{S}_2)^{2-}$ (the $[\text{Fe}-\text{SS}-\text{Fe}]^+$ cis chain at top right). Subsequent oxidation leads to a pyrite-like Fe-SS-Fe chain with Raman observable polysulfide (S_2^{2-}).

in Fe^{3+} containing rhombs and chain isomers (observable by XANES). The lower energy $[\text{FeSFeS}]^+$ chain isomer consists of multiple rotamers, which upon rotation of the common FeS bond, generates the $[\text{FeSSFe}]^+$ chain isomer leading to S-S bond formation and an intra-molecular redox shift, when the minimum distance between the sulfurs is reached (top right of Fig. 7B). Following this change in the redox locus, a second one electron oxidation to a polysulfide containing species is indicated by new Raman vibrational modes $\leq 253 \text{ cm}^{-1}$.

The free energy differences depicted in Fig. 7A do not allow for a facile interconversion between the ligand-free, coordinatively unsaturated diiron persulfides and $[2\text{Fe}-2\text{S}]$ rhombs under ambient conditions. However, when considering hydrothermal conditions, free energy differences of 100 kJ mol^{-1} can be readily overcome. Furthermore, addition of metal-terminal ligand bonds to the redox active moiety (to the dangling Fe^{2+} ions with $\Delta G_r^\circ \sim 100 \text{ kJ mol}^{-1}$) or embedding the rhombs and chains into a mineral/nanoparticle environment is expected to considerably decrease the free energy of interconversion and thus flatten the potential energy surface. The metal- and ligand-based oxidation cycles may thus become energetically balanced, which provides the energetic rationale for the simultaneous presence of oxidized and reduced metals and ligands seen in our experiments.

As ligand-based oxidation requires a structural rearrangement of two sulfide moieties (Fig. 7, $[2\text{Fe}-2\text{S}]$ rhomb \rightarrow $[\text{FeSSFe}]^{2+}$ chain), metal-based oxidation likely occurs more readily, with the oxidation of iron preceding the oxidation of sulfide. Variability in the pathway energies could allow electro-

chemical promotion of these oxidation routes, altering the stoichiometry of x and y in $\text{Fe}^{2+}_{1-3x}\text{Fe}^{3+}_{2x}\text{S}^{2-}_{1-y}(\text{S}_n^{2-})_y$. As the reduction of elemental sulfur (produced after the oxidation of polysulfides in A3 or their disproportionation) back to sulfide was observed in our voltametric experiments with $n(\text{Fe}^{2+}\text{S}^{2-})_{(s)} + \text{Na}_2\text{S}_n$ in C2 (Fig. 2B), the ligand-based oxidations appear to be reversible under the here investigated electrode potential ranges. The reduction of ferric iron to ferrous iron also appears to be feasible, as the electrode potentials necessary for the reduction of the $^1[2\text{Fe}-2\text{S}]^{2+}/[2\text{Fe}-2\text{S}]^{1+}$ and $^2[2\text{Fe}-2\text{S}]^{1+}/[2\text{Fe}-2\text{S}]^0$ redox couples are calculated to be -0.31 V and $+0.13 \text{ V}$ vs. Ag/AgCl, respectively. Such reversibility would potentially permit continuous cycling through the metal- and ligand-based oxidation states by avoiding the decomposition of the electrode through e.g. the accumulation of iron polysulfide species, making $\text{Fe}^{2+}_{1-3x}\text{Fe}^{3+}_{2x}\text{S}^{2-}_{1-y}(\text{S}_n^{2-})_y$ suitable as an electrocatalyst.

Conclusions

We report the electrochemical synthesis of Fe^{3+} containing iron sulfide from freshly precipitated iron(II) sulfide under ambient conditions. Previously, temperatures above 70°C and the addition of oxidants, such as FeCl_3 or H_2S , were necessary to accomplish this transformation.²¹ The presence of ferric iron was indicated by a shift of the S K-edge XANES to lower energies from 2471.0 eV to 2470.2 eV and a Raman shift of the normal mode of $n(\text{Fe}^{2+}\text{S}^{2-})_{(s)}$ from 292 to 305 cm^{-1} at more

positive electrode potentials. The production of polysulfides from $\text{Fe}^{2+}\text{S}^{2-}_{(s)}$ is detected in cyclic voltammograms due to the oxidation of polysulfides to elemental sulfur at 0 V. With increasing the applied electric potential from -0.80 V to -0.35 V and further to 0 V, $n(\text{Fe}^{2+}\text{S}^{2-})_{(s)}$ exhibited increases in the Raman signal intensities at 253 cm^{-1} and at wavenumbers below 140 cm^{-1} , which are attributed to a progression of the oxidation of sulfide to polysulfides. These vibrational modes are proposed to originate from iron bound persulfides, as shown on the core-extracted $[\text{2Fe-2S}]$ in a persulfide ligand environment and model $[\text{2Fe-2S}]$ persulfide clusters respectively.

Fe^{3+} and S_n^{2-} containing mackinawite is a chemically distinct FeS phase that exhibits both a ligand- and metal-centered redox locus, through the oxidation of sulfide to polysulfides and Fe^{2+} to Fe^{3+} . Its oxidized form is expressed here as $\text{Fe}^{2+}_{1-3x}\text{Fe}^{3+}_{2x}\text{S}^{2-}_{1-y}(\text{S}_n^{2-})_y$ based on previous studies,³³ estimating the Fe^{3+} content (x) to be less than 0.1. Within the scope of this work, we could not determine the amount of polysulfides (y) as an additional oxidation product. Analogous to the $2e^-$ redox reactions of the model $[\text{2Fe-2S}]$ rhombs that mimic plant ferredoxins, $n(\text{Fe}^{2+}\text{S}^{2-})_{(s)}$ could act as a catalyst for reactions typically catalyzed by biological $[\text{Fe-S}]$ clusters.⁶⁷ Further investigations into the reversibility of both Fe^{2+} and S^{2-} oxidation are necessary, but the reduction of elemental sulfur, produced during voltametric experiments from polysulfides, and the calculated redox potentials for $^1[\text{2Fe-2S}]^{2+}$ and $^2[\text{2Fe-2S}]^{1+}$ rhombs suggest the reversibility of these redox reactions. The presence of both ferric iron and polysulfides suggests that this material could potentially produce either $\text{Fe}^{2+}\text{Fe}^{3+}_2\text{S}^{2-}_4$ (greigite) or $\text{Fe}^{2+}(\text{S}_2)^{2-}$ (pyrite) based on the applied electrode potential (see also ref. 68). By understanding how solution and electrode potentials could favor either metal- or ligand-oxidation, tunability of these reaction routes can be achieved and the resulting material can be tailored towards facilitating reactions typically promoted by either greigite or pyrite.

Author contributions

S.A.S., S.E.M. and R.K.Sz wrote the manuscript and conceptualized the presented work, S.A.S wrote the original manuscript, which was edited in initial rounds by R.K.Sz. and S.E.M.. S.A. S., S.E.M., R.K.Sz acquired, curated and validated the presented data. Y.L., N.K., S.M.W., T.Y assisted in the data acquisition and formal analysis. S.A.S., S.E.M., R.K.Sz, R.N, N.K. and S.M.W. developed the methodology concerning the data acquisition. Funding for this project and resources were acquired and supervision provided by S.E.M., R.K.Sz, and M.H. All authors reviewed and edited this work prior to submission.

Data availability statement

In order to accelerate the dissemination of our work, reference Raman and XANES spectra, as well as a full documentation of

the computational results were uploaded online to a public depository Zenodo. The experimental data presented here is deposited under the following DOI: 10.5281/zenodo.5056738 and can be accessed via <https://zenodo.org/record/5056738>.

Conflicts of interest

There are no conflicts to declare.

Acknowledgements

The authors would like to thank Jean-François Gaillard (Northwestern University, U.S.A.) for his assistance with the usage of the XAS software used during the analysis. We are especially grateful to Hooman Hosseinkhannazer (Norcada) and Yuke Yamaguchi (LxRay) for consultation about the beam line experiments and providing x-ray windows used in sample analysis. S.A.S. acknowledges a graduate scholarship received from the Ministry of Education, Culture, Sports, Science and Technology (MEXT) of Japan. S.E.M. acknowledges support by NSF award #1724300. Use of the Stanford Synchrotron Radiation Lightsource, SLAC National Accelerator Laboratory, is supported by the U.S. Department of Energy, Office of Science, Office of Basic Energy Sciences under Contract No. DE-AC02-76SF00515. The SSRL Structural Molecular Biology Program is supported by the DOE Office of Biological and Environmental Research, and by the National Institutes of Health, National Institute of General Medical Sciences (P30GM133894). The contents of this publication are solely the responsibility of the authors and do not necessarily represent the official views of NIGMS or NIH. Access to CCDB and ICSD crystal structures databases and subsequent computational research was supported by the U.S. Department of Energy, Office of Science, Basic Energy Sciences under Award DESC0020246 (R.K.Sz.).

Notes and references

- 1 G. W. Luther, B. T. Glazer, L. Hohmann, J. I. Popp, M. Taillefert, T. F. Rozan, P. J. Brendel, S. M. Theberge and D. B. Nuzzio, *J. Environ. Monit.*, 2001, **3**, 61–66.
- 2 R. A. Berner, *Am. J. Sci.*, 1970, **268**, 1–23.
- 3 M. S. Faber, M. A. Lukowski, Q. Ding, N. S. Kaiser and S. Jin, *J. Phys. Chem. C*, 2014, **118**, 21347–21356.
- 4 B. Konkena, K. Junge Puring, I. Sinev, S. Piontek, O. Khavryuchenko, J. P. Dürholt, R. Schmid, H. Tüysüz, M. Muhler, W. Schuhmann and U.-P. Apfel, *Nat. Commun.*, 2016, **7**, 12269.
- 5 G. Wächtershäuser, *Syst. Appl. Microbiol.*, 1988, **10**, 207–210.
- 6 W. Heinen and A. M. Lauwers, *Origins Life Evol. Biospheres*, 1996, **26**, 131–150.
- 7 M. J. Russell and W. Martin, *Trends Biochem. Sci.*, 2004, **29**, 358–363.

- 8 C. Huber and G. Wächtershäuser, *Science*, 1997, **276**, 245–247.
- 9 M. A. A. Schoonen, Y. Xu and J. Bebie, *Origins Life Evol. Biospheres*, 1999, **29**, 5–32.
- 10 M. Dörr, J. Käßbohrer, R. Grunert, G. Kreisel, W. A. Brand, R. A. Werner, H. Geilmann, C. Apfel, C. Robl and W. Weigand, *Angew. Chem., Int. Ed.*, 2003, **42**, 1540–1543.
- 11 A. D. Gordon, A. Smirnov, S. L. Shumlas, S. Singireddy, M. DeCesare, M. A. A. Schoonen and D. R. Strongin, *Origins Life Evol. Biospheres*, 2013, **43**, 305–322.
- 12 C. Bonfio, L. Valer, S. Scintilla, S. Shah, D. J. Evans, L. Jin, J. W. Szostak, D. D. Sasselov, J. D. Sutherland and S. S. Mansy, *Nat. Chem.*, 2017, **9**, 1229–1234.
- 13 N. Kitadai, R. Nakamura, M. Yamamoto, K. Takai, Y. Li, A. Yamaguchi, A. Gilbert, Y. Ueno, N. Yoshida and Y. Oono, *Sci. Adv.*, 2018, **4**, eaao7265.
- 14 M. Preiner, K. Igarashi, K. B. Muchowska, M. Yu, S. J. Varma, K. Kleinermanns, M. K. Nobu, Y. Kamagata, H. Tüysüz, J. Moran and W. F. Martin, *Nat. Ecol. Evol.*, 2020, **4**, 534–542.
- 15 R. Hudson, R. de Graaf, M. S. Rodin, A. Ohno, N. Lane, S. E. McGlynn, Y. M. A. Yamada, R. Nakamura, L. M. Barge, D. Braun and V. Sojo, *Proc. Natl. Acad. Sci. U. S. A.*, 2020, **117**, 22873–22879.
- 16 S. A. Sanden, R. Yi, M. Hara and S. E. McGlynn, *Chem. Commun.*, 2020, **56**, 11989–11992.
- 17 D. Rickard and G. W. Luther, *Chem. Rev.*, 2007, **107**, 514–562.
- 18 R. Guilbaud, I. B. Butler, R. M. Ellam and D. Rickard, *Earth Planet. Sci. Lett.*, 2010, **300**, 174–183.
- 19 G. W. Luther and D. T. Rickard, *J. Nanopart. Res.*, 2005, **7**, 389–407.
- 20 A. Matamoros-Velozá, O. Cespedes, B. R. G. Johnson, T. M. Stawski, U. Terranova, N. H. de Leeuw and L. G. Benning, *Nat. Commun.*, 2018, **9**, 3125.
- 21 A. Roldan, N. Hollingsworth, A. Roffey, H.-U. Islam, J. B. M. Goodall, C. R. A. Catlow, J. A. Darr, W. Bras, G. Sankar, K. B. Holt, G. Hogarth and N. H. de Leeuw, *Chem. Commun.*, 2015, **51**, 7501–7504.
- 22 S. Schouten, G. B. van Driel, J. S. Damsté and J. W. de Leeuw, *Geochim. Cosmochim. Acta*, 1993, **57**, 5111–5116.
- 23 M. R. Raven, A. L. Sessions, J. F. Adkins and R. C. Thunell, *Geochim. Cosmochim. Acta*, 2016, **190**, 175–190.
- 24 A. Picard, A. Gartman and P. R. Girguis, *Astrobiology*, 2021, **21**(5), 587–604.
- 25 G. W. Luther, *Geochim. Cosmochim. Acta*, 1991, **55**, 2839–2849.
- 26 D. T. Rickard, *Am. J. Sci.*, 1975, **275**, 636–652.
- 27 A. R. Lennie, S. A. T. Redfern, P. E. Champness, C. P. Stoddart, P. F. Schofield and D. J. Vaughan, *Am. Mineral.*, 1997, **82**, 302–309.
- 28 D. Rickard and G. W. Luther, *Geochim. Cosmochim. Acta*, 1997, **61**, 135–147.
- 29 L. M. White, R. Bhartia, G. D. Stucky, I. Kanik and M. J. Russell, *Earth Planet. Sci. Lett.*, 2015, **430**, 105–114.
- 30 H. Wada, *BCSJ*, 1977, **50**, 2615–2617.
- 31 S. Boursiquot, M. Mullet, M. Abdelmoula, J.-M. Génin and J.-J. Ehrhardt, *Phys. Chem. Min.*, 2001, **28**, 600–611.
- 32 J.-A. Bourdoiseau, M. Jeannin, R. Sabot, C. Rémazeilles and Ph. Refait, *Corros. Sci.*, 2008, **50**, 3247–3255.
- 33 M. Mullet, S. Boursiquot, M. Abdelmoula, J.-M. Génin and J.-J. Ehrhardt, *Geochim. Cosmochim. Acta*, 2002, **66**, 829–836.
- 34 Y. Sano, A. Kyono, Y. Yoneda, N. Isaka, S. Takagi and G. Yamamoto, *J. Mineral. Petrol. Sci.*, 2020, **115**(3), 261–275.
- 35 J.-A. Bourdoiseau, M. Jeannin, C. Rémazeilles, R. Sabot and P. Refait, *J. Raman Spectrosc.*, 2011, **42**, 496–504.
- 36 D. Rickard, *Stockholm Contrib. Geol.*, 1969, **20**, 67–95.
- 37 M. A. A. Schoonen and H. L. Barnes, *Geochim. Cosmochim. Acta*, 1991, **55**, 1505–1514.
- 38 R. T. Wilkin and H. L. Barnes, *Geochim. Cosmochim. Acta*, 1996, **60**, 4167–4179.
- 39 A. Kamyshny, A. Goifman, J. Gun, D. Rizkov and O. Lev, *Environ. Sci. Technol.*, 2004, **38**, 6633–6644.
- 40 S. M. Webb, *Phys. Scr.*, 2005, **115**, 1011.
- 41 B. Ravel and M. Newville, *J. Synchrotron Radiat.*, 2005, **12**, 537–541.
- 42 F. Weigend and R. Ahlrichs, *Phys. Chem. Chem. Phys.*, 2005, **7**, 3297–3305.
- 43 A. D. Becke, *Phys. Rev. A*, 1988, **38**, 3098–3100.
- 44 J. P. Perdew, *Phys. Rev. B: Condens. Matter Mater. Phys.*, 1986, **33**, 8822–8824.
- 45 M. J. Frisch, G. W. Trucks, H. B. Schlegel, G. E. Scuseria, M. A. Robb, J. R. Cheeseman, G. Scalmani, V. Barone, G. A. Petersson, H. Nakatsuji, X. Li, M. Caricato, A. V. Marenich, J. Bloino, B. G. Janesko, R. Gomperts, B. Mennucci, H. P. Hratchian, J. V. Ortiz, A. F. Izmaylov, J. L. Sonnenberg, D. Williams-Young, F. Ding, F. Lipparini, F. Egidi, J. Goings, B. Peng, A. Petrone, T. Henderson, D. Ranasinghe, V. G. Zakrzewski, J. Gao, N. Rega, G. Zheng, W. Liang, M. Hada, M. Ehara, K. Toyota, R. Fukuda, J. Hasegawa, M. Ishida, T. Nakajima, Y. Honda, O. Kitao, H. Nakai, T. Vreven, K. Throssell, J. A. Montgomery Jr., J. E. Peralta, F. Ogliaro, M. J. Bearpark, J. J. Heyd, E. N. Brothers, K. N. Kudin, V. N. Staroverov, T. A. Keith, R. Kobayashi, J. Normand, K. Raghavachari, A. P. Rendell, J. C. Burant, S. S. Iyengar, J. Tomasi, M. Cossi, J. M. Millam, M. Klene, C. Adamo, R. Cammi, J. W. Ochterski, R. L. Martin, K. Morokuma, O. Farkas, J. B. Foresman and D. J. Fox, *Gaussian 16, Revision C.01*, Gaussian, Inc, Wallingford CT, 2016.
- 46 A. V. Marenich, C. J. Cramer and D. G. Truhlar, *J. Phys. Chem. B*, 2009, **113**, 6378–6396.
- 47 F. L. Hirshfeld, *Theor. Chim. Acta*, 1977, **44**, 129–138.
- 48 R. S. Mulliken, *J. Chem. Phys.*, 1955, **23**, 1833–1840.
- 49 D. Rickard, *Geochim. Cosmochim. Acta*, 2006, **70**, 5779–5789.
- 50 A. J. Bard, R. Parsons and J. Jordan, *Standard Potentials in Aqueous Solution*, CRC Press, 1985.
- 51 A. N. Buckley, I. C. Hamilton and R. Woods, *J. Electroanal. Chem. Interf. Electrochem.*, 1987, **216**, 213–227.

- 52 M. A. Aziz, M. Sohail, M. Oyama and W. Mahfoz, *Electroanalysis*, 2015, **27**, 1268–1275.
- 53 Y. Gorlin, A. Siebel, M. Piana, T. Huthwelker, H. Jha, G. Monsch, F. Kraus, H. A. Gasteiger and M. Tromp, *J. Electrochem. Soc.*, 2015, **162**, A1146.
- 54 T. A. Pascal, C. D. Pemmaraju and D. Prendergast, *Phys. Chem. Chem. Phys.*, 2015, **17**, 7743–7753.
- 55 K. R. Williams, B. Hedman, K. O. Hodgson and E. I. Solomon, *Inorg. Chim. Acta*, 1997, **263**, 315–321.
- 56 T. Glaser, K. Rose, S. E. Shadle, B. Hedman, K. O. Hodgson and E. I. Solomon, *J. Am. Chem. Soc.*, 2001, **123**, 442–454.
- 57 A. Baum, A. Milosavljević, N. Lazarević, M. M. Radonjić, B. Nikolić, M. Mitschek, Z. I. Maranloo, M. Šćepanović, M. Grujić-Brojčin, N. Stojilović, M. Opel, A. Wang, C. Petrovic, Z. V. Popović and R. Hackl, *Phys. Rev. B*, 2018, **97**, 054306.
- 58 P. L. Polavarapu, *J. Phys. Chem.*, 1990, **94**, 8106–8112.
- 59 D. Michalska and R. Wysockiński, *Chem. Phys. Lett.*, 2005, **403**, 211–217.
- 60 Y. E. Mendili, B. Minisini, A. Abdelouas and J.-F. Bardeau, *RSC Adv.*, 2014, **4**, 25827–25834.
- 61 D. Coucouvanis, D. Swenson, P. Stremple and N. C. Baenziger, *J. Am. Chem. Soc.*, 1979, **101**, 3392–3394.
- 62 G. J. Janz, J. W. Coutts, J. R. Downey and E. Roduner, *Inorg. Chem.*, 1976, **15**, 1755–1759.
- 63 W. Buckel and R. K. Thauer, *Front. Microbiol.*, 2018, **9**, 401.
- 64 B. Li and S. J. Elliott, *Electrochim. Acta*, 2016, **199**, 349–356.
- 65 W. Thamer, I. Cirpus, M. Hans, A. J. Pierik, T. Selmer, E. Bill, D. Linder and W. Buckel, *Arch. Microbiol.*, 2003, **179**, 197–204.
- 66 J. M. Lambert, G. Simkovich and P. L. Walker, *Fuel*, 1980, **59**, 687–690.
- 67 H. Beinert, R. H. Holm and E. Münck, *Science*, 1997, **277**, 653–659.
- 68 S. Hunger and L. G. Benning, *Geochem. Trans.*, 2007, **8**, 1–20.